HHS Public Access

Author manuscript

ACS Nano. Author manuscript; available in PMC 2019 April 24.

Published in final edited form as:

ACS Nano. 2018 April 24; 12(4): 3699–3713. doi:10.1021/acsnano.8b00893.

Magnetic Particle Imaging Guided Heating In Vivo using Gradient Fields For Arbitrary Localization of Magnetic Hyperthermia Therapy

Zhi Wei Tay[†], **Prashant Chandrasekharan**[†], **Andreina Chiu-Lam**[‡], **Daniel W. Hensley**[¶], **Rohan Dhavalikar**[‡], **Xinyi Y. Zhou**[†], **Elaine Y. Yu**[¶], **Patrick W. Goodwill**[¶], **Bo Zheng**[†], **Carlos Rinaldi**[‡], and **Steven M. Conolly**[†,§]

[†]University of California Berkeley, Department of Bioengineering, Berkeley, CA 94720, United States

[‡]University of Florida, Department of Chemical Engineering, Gainesville, FL 32611, United States

[¶]Magnetic Insight, Inc., Alameda, CA 94501, United States

[§]Department of Electrical Engineering and Computer Sciences, University of California, Berkeley, CA 94720, United States

Abstract

Image guided treatment of cancer enables physicians to localize and treat tumors with great precision. Here, we present *in vivo* results showing that an emerging imaging modality, Magnetic Particle Imaging (MPI), can be combined with Magnetic Hyperthermia into a image-guided theranostic platform. MPI is a noninvasive 3D tomographic imaging method with high sensitivity and contrast, zero ionizing radiation, and is linearly quantitative at any depth with no view limitations. The same superparamagnetic iron oxide nanoparticle (SPIONs) tracers imaged in MPI can also be excited to generate heat for magnetic hyperthermia. In this study, we demonstrate a theranostic platform, with quantitative MPI image-guidance for treatment planning and use of the MPI gradients for spatial localization of magnetic hyperthermia to arbitrarily selected regions. This addresses a key challenge of conventional magnetic hyperthermia - SPIONs delivered systemically accumulate in off-target organs (*e.g.*, liver and spleen), and difficulty in localizing hyperthermia results in collateral heat damage to these organs. Using a MPI-magnetic hyperthermia workflow, we demonstrate image-guided, spatial localization of hyperthermia to the tumor while minimizing collateral damage to the nearby liver (1 – 2 cm distant). Localization of thermal damage and therapy was validated with luciferase activity and histological assessment. Apart from localizing thermal therapy, the technique presented here can also be extended to localize actuation of drug release and other biomechanical-based therapies. With high contrast and high sensitivity imaging combined with precise control and localization of the actuated therapy, MPI is a powerful platform for magnetic-based theranostics.

Graphical abstract

zwtay@berkeley.edu, Phone: +1 (678) 4801284.

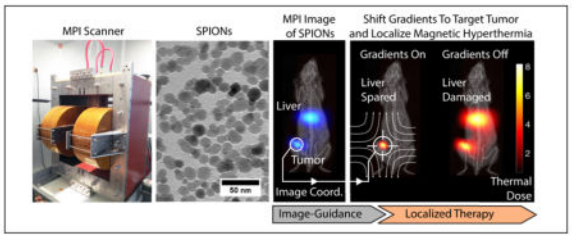

Keywords

Magnetic Particle Imaging; Magnetic Nanoparticles; Superparamagnetic Iron Oxide Nanoparticles; Magnetic Hyperthermia; Magnetic Fluid Hyperthermia; Image-guided; Theranostics; Targeted Therapy

The ideal image-guided treatment of tumors aims to treat only the cancer cells while minimizing damage to surrounding tissue. Magnetic hyperthermia is a promising approach that has the potential for real-time image-guidance while reaching deep tissues without invasive catheters. This approach relies on delivery of magnetic nanoparticles to tumors, followed by application of alternating magnetic fields (AMF) that fully penetrate the human body without depth limitations.[1,2] This causes the Superparamagnetic Iron Oxide Nanoparticles (SPIONs) to generate and release heat to their environment.[3–6] This approach has many advantages: First, SPIONs are regarded as biocompatible and biodegradable[7,8] *in vivo*. Second, heating is localized to the SPION biodistribution. Third, magnetic hyperthermia has greater synergy with chemical therapies[9–13] than other forms of hyperthermia. Fourth, magnetic hyperthermia has also been shown to induce anti-tumor immunity[14,15] and can kill cancer cells without a macroscopic temperature rise. Lastly, instrumentation already exists[16] to generate AMFs suitable for SPION-based thermal therapy in patients.

However, magnetic hyperthermia has several challenges to address. First and foremost, SPIONs delivered systemically accumulate in off-target organs (*e.g.*, liver and spleen), resulting in collateral damage[17] to these organs. Current approaches to actuate SPION heating do not permit spatial control with precision required to spare healthy organs while treating tumors. While magnetic hyperthermia is inherently localized to the SPION distribution, there is no current way to target magnetic energy to only a local subset of the SPION distribution arbitrarily deep in the body. This is a problem since the non-specific uptake of even antibody-targeted SPIONs is far higher in the excretory organs (liver, spleen, or kidneys) than in the targeted region such as the tumor,[18] indiscriminate magnetic heating of all the nanoparticles in the body will result in collateral damage to healthy tissues. Strategies to focus the excitation wave (300 – 700 kHz) are fundamentally limited by diffraction, regardless of the number of external coils employed, to a spot size of about half the *in vivo* wavelength (~ 50 m)[1,19] and is thus untenable for clinical applications. Other strategies to localize the excitation using surface coils work poorly at depth due to field amplitude fall-off of the excitation wave.

In addition, some other challenges are quantitative imaging of SPION mass for hyperthermia treatment planning. Due to relatively high SPION doses required for heating, for this case, quantification with Magnetic Resonance Imaging (MRI) is difficult since the SPION effect on the MRI Transverse Relaxation Time - Star (T2*) saturates. We currently lack non-invasive methods of monitoring temperature rise around the SPION for deep tumors, and it is difficult to use MR Thermometry in regions close to the SPIONs.[20]

To address these challenges, we propose the use of Magnetic Particle Imaging (MPI) for image-guidance and the use of strong magnetic gradient fields inherent in MPI systems to provide user-defined, arbitrary localization of magnetic hyperthermia. Fig. 1 uses experimental data to depict the theranostic workflow proposed.

First developed in 2005 by Gleich and Weizenecker,[21] MPI is an emerging tracer-based molecular imaging technique that directly detects and quantifies the non-linear magnetization of superparamagnetic iron oxide (SPION) tracers.[22–26] As in other molecular imaging techniques, like nuclear medicine, there is no signal from background tissue in MPI, giving MPI images high image contrast for SPION tracers. This good contrast mechanism, combined with the use of low-frequency magnetic fields and clinically safe magnetic tracers, enables MPI to produce clinical-grade images with zero tissue signal attenuation and high image sensitivity. [21,27] Unlike Magnetic Resonance Imaging (MRI), safety in MPI is bound by magnetostimulation and specific absorption rate (SAR) safety limitations.[28] MPI is best compared to gold-standard tracer imaging techniques, such as nuclear medicine, but without the limitations of radiation safety or radionuclide half-life for longitudinal imaging. As such, MPI shows excellent promise for clinical applications such as angiography,[29] stem cell tracking and vitality assessment,[30–32] brain perfusion,[33] lung perfusion,[34] lung ventilation,[35] cancer imaging,[36] gut bleed detection[37] and hyperthermia.[1,38,39]

MPI has several intrinsic advantages. First, MPI has been shown to be a highly sensitive tracer modality with near picogram sensitivity.[40–42] MPI has high temporal resolution, with real-time MPI image-guidance of catheters demonstrated.[43,44] Temporal resolutions of 46 frames per second have been shown in recent state-of-the-art scanners.[45] Next, MPI has been demonstrated to be high-contrast (no tissue signal unlike MRI) and quantitative for the SPION mass[30,31,36,45,46] therefore allowing prediction of specific absorption rate (SAR) dose from an image of the SPIONs.

Magnetic Particle Imaging works by exploiting the nonlinear magnetization of the SPION tracers used. Strong magnetic field gradients magnetically saturate the SPIONs everywhere except the SPIONs within the field-free-region (FFR). Only these unsaturated tracers at the FFR are able to respond to a small excitation magnetic field (20 kHz 20 mT). MPI can be considered a (magnetic) sensitive point method, and scans a 3D volume by rastering the sensitive FFR point around (Fig. 2). Image reconstruction[23,27] and hardware[47–49] are detailed in prior work.

The physics underlying MPI is thus very similar to the physics underlying magnetic hyperthermia, which makes MPI an ideal candidate for resolving some of the challenges

mentioned above. For example, the exact same nanoparticle core generates the MPI signal as well as the heat for magnetic hyperthermia.[50] The issue of the imaging label separating from the therapeutic core is thus non-existent. Furthermore, the same physical mechanism (rotation of magnetic moment) that generates signal in MPI generates heating in magnetic hyperthermia, thus giving the MPI-predicted heating strong predictive power. [38,39]

This MPI-magnetic hyperthermia similarity can be further exploited to localize heating. Unlike prior strategies that try to shape the excitation field or use surface coils for heat localization, as shown in Fig. 3 we use a completely different mechanism of gradient magnetic fields where heat is localized to the narrow axis of the field-free-line (FFL). Because the signal generation mechanism in MPI and the heat generation mechanism of magnetic hyperthermia are the same - both rely on nanoparticle magnetic dipole rotation, the MPI gradients (hardware) that are used to localize MPI signal in MPI imaging by rendering all but one location unresponsive to MPI excitation, can also be used for localization of magnetic hyperthermia heating. This gradient-based mechanism can also be understood as magnetically locking the nanoparticles in place (magnetic saturation) and preventing rotation to generate heat or MPI signal. Only the central region of the gradient field with zero magnitude lacks this suppression, therefore localizing the MPI signal or magnetic hyperthermia heating. This can also be understood by SPION hysteresis curves at different positions in the gradient. Hysteresis in the dynamic magnetization curves occur due to relaxation effects[50,51] and heating is related to the area in the M-H plot bounded by this curve. The spatially-variable saturating effect is observed by the hysteresis curves becoming narrower as the SPION is moved away from the field-free-region (see Fig. 4). The hardware to shift and control the location of this zero field point (field-free-line) is already present in MPI scanners.[30,37,45,47] The same imaging hardware for MPI which rasters the signal localization spot about the field-of-view to generate an image, can be utilized in magnetic hyperthermia to localize heat to user-selected regions by designing a shift-and-park trajectory to visit and heat selected thermal therapy targets in turn.

This proposed MPI-gradient method enables precise thermal dose localization with high spatial resolution. Precision of the localization improves with higher MPI gradient strength, thus offering an avenue towards high-spatial-precision thermal therapy. We achieved ~ 7 mm (full-width-half-maximum) spatio-thermal resolution with a 2.35 T/m MPI gradient and expect ~ 2.35 mm with a 7 T/m MPI gradient based on previous imaging and theory results[52]).

As such, we can envision a theranostic workflow where an MPI image is first taken and the same MPI gradients are subsequently used to target and localize SPION heating in the therapy stage as shown in Fig. 1. To ensure heating only in the magnetic hyperthermia stage and not in the diagnostic/imaging stage, a very low frequency (20 kHz) is used for MPI imaging. The strong frequency dependence of magnetic hyperthermia[50] means that SPIONs do not heat during MPI imaging, and heat only when in ‘therapy mode’ at 354 kHz. Imaging also uses a raster trajectory, thus the net energy deposited at any location in the body is very low because each location is only scanned for a few milliseconds. Prior studies have started to investigate the effect of frequency on magnetic hyperthermia heating[50] as well as the use of gradients to localize heating *in vitro* [1,19] and *in vivo*.[53] We expand upon prior work and

combine all the elements to perform an in-vivo demonstration of MPI image-guidance for localization heating *and therapy* in the context of a rodent cancer model.

Results and Discussion

User-defined, Arbitrary Localization of Heating *In Vitro*

Fig. 5 shows the *in vitro* results obtained from a 3 × 3 phantom undergoing the theranostic workflow illustrated in Fig. 1. During the initial MPI imaging scan, negligible heating is observed. This is because each nanoparticle is interrogated/excited very briefly due to the raster imaging trajectory. In addition, a low frequency of 20 kHz is used. In contrast, the heating mode of the MPI-magnetic hyperthermia system generates > 10°C of heating over the same time of the MPI scan. Without the MPI gradients, all the wells in the phantom are heated up equally. This is also different from the MPI scan because the entire region of nanoparticles is continuously excited for the entire duration and a higher excitation frequency is used. Finally, by putting the MPI gradients in place, a field-free-line is generated and heating can be localized to that line. From the MPI image, one of the 9 vials is chosen. We chose the central vial to demonstrate that all other neighboring vials do not heat up. As shown in the results, negligible heating is observed in all wells except the targeted well. In addition, this heating location can be arbitrarily moved to another well simply by shifting the location of the field-free-line that is under the control of the MPI gradients. This demonstrates arbitrary control of heating location. Lastly, the 3 × 3 phantom has the wells spaced 7 mm apart. The results demonstrate that for a 2.35 T/m gradient used, heating can be localized to within a 7 mm radius. Stronger MPI gradients narrow the ‘heating spot size’ linearly with the gradient strength. If higher MPI gradients such as the 7 T/m gradient reported in a recent MPI on small animals[37] are used, heat localization is expected to improve to < 2.35 mm.

Image-guided, Arbitrary Localization of Heating *In Vivo*

In Fig. 1, we show experimental *in vivo* data in a xenograft athymic mouse model outlining the ideal theranostics workflow *in vivo* or in the clinic. In this experiment, we show that we are able to image the biodistribution of the SPIONs in an animal, segment the regions that we wish to heat, estimate the thermal dose required due to the quantitative nature of MPI imaging *in vivo*, and then apply a highly localized heat dose only to locations in a tumor. This is done while sparing nearby healthy tissues that may have non-specific accumulations of nanoparticles, or the body’s natural clearance organs for these SPIONs, such as the liver or spleen. These clearance organs are sensitive to heat damage and can be affected from alternating magnetic field (AMF) heating as evidenced in prior work.[17,54]

The results shown in Fig. 6 for the experimental group 1 (SPIONs injected into the single tumor as well as tail vein for clearance to liver) confirm that the *in vitro* localization can be replicated *in vivo*. Similar to the *in vitro* experimental series, first, we verify that there is negligible heating during the MPI scan. Second, when the MPI gradients are turned off and the entire volume is excited at 354 kHz, indiscriminate heating occurs at all locations with SPIONs. Heating of the SPIONs cleared to the liver is observed at the same time as the heating of the tumor. Tumor and liver temperatures of $43°C$ were reached in only 12

minutes. A control mouse with saline instead of SPIONs was also subject to the same uniform AMF but showed no increase in tumor and liver temperatures, verifying that this indiscriminate heating is not a result of non-specific SAR from AMF interacting with biological tissue. Next, the MPI gradients are turned on and we observe that the liver is spared from heating while only the tumor is heated. Lastly, we use a dual tumor mouse to demonstrate arbitrary control of the heating location. Initially, the bottom tumor is targeted and the results show localized heating in the bottom tumor but not the top tumor. Then, the field-free-line is shifted to the top tumor and the results show heating in the top tumor but not the bottom. These results show that with MPI gradients, the user can arbitrary control the location of heating. With guidance from the initial MPI image, the treatment planning can design a "heating trajectory" for the field-free-line or field-free-point and therefore spare healthy organs such as the liver from collateral damage.

Dose Planning and Heat Localization *In Vivo*

MPI has a few key characteristics that allow for thermal dose planning. First, MPI is a quantitative imaging modality and is able to accurately image the amount of the iron or SPION *in vivo*. This has been extensively validated by prior work.[31,36,46] Second, because the exact same nanoparticle core generates the MPI signal as well as the magnetic hyperthermia heat, the MPI signal is predictive for thermal energy deposition. Issues of the imaging label separating from the therapeutic core are thus non-existent. Because the thermal energy deposited is linearly related to the amount of SPIONs, by accurately quantifying the amount of SPIONs *in vivo*, the expected thermal energy deposited can be directly calculated. This can be clearly seen by the fact that thermal efficiency is often calculated by the SAR of the magnetic particles used in units of W/g of particles.

In Fig 7, we experimentally validate these key characteristics of MPI. In Fig 7.a, we verify that with our field-free-line scanner, MPI is quantitative for the amount of iron even when projection images are taken. In Fig 7.b, we correlate the SAR deposited (proportional to the initial temperature rise measured when the 354 kHz excitation is initiated) to the MPI image intensity. Our results show that MPI pixel intensity (linear with mass of SPION) is well correlated with the initial dT/dt and local SAR ($R^2 = 0.964$). The MPI image is thus invaluable for thermal dose planning, underscoring the theranostics potential of MPI for image guided thermal therapy.

Lastly, in Fig 7.c, we demonstrate statistics showing localization of heating to the target location ($p < 0.001$, $n = 14$) and that minimal heating is observed at non-target locations even if SPIONs are present. This is clearly attributed to the presence of the MPI gradient and field-free-line as no heat localization is observed when the MPI gradient is absent.

These results taken together shows that MPI can be very useful in clinical situations where non-specific uptake of therapeutics is an issue. With gradient-based localization of actuation (heat), MPI enables extremely localized and precise treatment even when the biological specificity of the therapeutic is not high and collateral damage to healthy parts of the body needs to be avoided. This relaxes the requirements for biological specificity and enables higher doses because actuation of therapy can be specific rather than indiscriminate.

Predictive Algorithm for the *In Vivo* Distribution of Heating

Here, we demonstrate the process behind estimating the thermal dose required as well as predicting the effectiveness of MPI-gradient spatial localization to verify if sensitive organs will be affected by the designed magnetic hyperthermia scan. Using this method, we can potentially simulate different target locations for the best region to target the MPI gradients to maximize tumor heating while avoiding nearby sensitive organs such as the liver.

To develop a predictive algorithm, we first calibrate the localization point-spread-function for heating due to the MPI gradient as well as the heat spread point-spread-function at steady-state (for a small point-source of heated SPIONs in an agarose gel phantom). This needs only be done once per MPI device. Mathematically as shown in Fig. 8, we would take the SAR image measured from the MPI SPION biodistribution image, then dot multiply it with the MPI gradient localization point-spread-function (centered at the target heating location). Subsequently, the gradient-narrowed SAR image is then convolved with the temperature spatial-point-spread-function to obtain a temperature rise image. This PSF was measured at temperature steady-state in an agarose phantom (no convective cooling) with constant heating of the point source. This PSF represents the worst-case spread of temperature rise (agarose is similar to a dead tissue phantom). The convective cooling from the blood perfusion in *vivo* will narrow this spread (assuming the blood pool represents a thermal sink). As such, the 10% boundary marked represents the worst case temperature spatial profile and in reality, the temperature rise *in vivo* should be constrained to a smaller region. The results from the forward model shown in the diagram match the experimental results in that no temperature rise was observed in the liver, which is outside the predicted temperature rise boundary. As such, this forward model based on worst-case heat-spread will be useful, albeit being quite conservative, for clinicians whose main aim is to avoid any damage to healthy organs and therefore would like to leave a large buffer region for safety.

Luciferase Assay shows Localized Therapy *In Vivo*

Assessment of treatment response was carried out on experimental groups 3 and 4 that have dual tumors of human triple negative breast cancer, MDA-MB-231-Luc. The luciferase expression in the tumors was measured before and after treatment, and used to evaluate the treatment response. The *in vivo* experimental results show > 7°C heating of the targeted tumor while the other tumor was negligibly heated (Fig. 9). Heating was maintained to achieve a Cumulative Equivalent Minutes at $43°C$ (CEM43) of greater than 70 minutes in order to observe any discernible treatment response.[55–57] The luciferase activity reduced considerably (~ 10-fold) in the treated tumor compared to the non-treated tumor. The luciferase activity confirms the thermal dose was selectively deposited on the tumor and resulted in majority of the luciferase-competent tumor cells dying.

Histological Assessment Verifies Localization of Thermal Damage to Target Region Only

Apoptosis in organs as a result of thermal damage was measured by quantification of the single and double stranded DNA breaks (TUNEL staining). Percentage apoptosis was calculated by dividing the number of TUNEL stained cells by the total number of cells (DAPI stain). From the histology images, > 50% of cells have undergone apoptosis in the tumors targeted with magnetic hyperthermia while no tissue damage was observed in off-

target tumors (Fig. 10.a). Experimental replicates (n=3) show localization of damage to the target region and protection of the off-target regions (Fig. 10.b). To evaluate the protective effect of gradient-based heat localization on minimizing collateral damage to the liver, we compared the liver from a mouse subject to uniform heating (no MPI gradients) as opposed to a mouse subject to gradient-localized heating (heating targeted at tumor and away from the liver). The results (Fig. 10.a) show visible damage to the liver when MPI gradients are absent while there is negligible damage when MPI gradients are present, confirming that MPI gradient-based localization of heating can indeed minimize collateral damage to clearance organs such as the liver. Presence of SPIONs in both the liver and tumor was verified by Prussian Blue staining (Fig. 10.c). This verifies that there is indeed clearance of SPIONs to the liver and that it can potentially be damaged by magnetic hyperthermia in the absence of the spatial localization gradients.

Discussion

Precision of Localization Linearly Improves with Gradient Strength

Image guided tumor ablation aims to kill 100% of tumor cells with minimal destruction of adjacent healthy tissue. The unavoidable dead region at the tumor periphery is termed the tumor margins and 2-mm margins are considered standard in clinical practice. In this work, we experimentally demonstrated a radial margin of ~ 7 mm on a 2.35 T/m gradient. Because spatial precision improves linearly with gradient strength, increasing the magnetic hyperthermia gradient strength to 7 T/m will improve precision to 2.35 mm which is very close to the 2 mm objective. This level of precision should be more than adequate to avoid heating healthy sites such as the liver while targeting various lesions. With electromagnet gradients, the gradient strength can be adapted to the clinical situation. Lower gradients allows more efficient heating of larger lesions while higher gradients can improve precision when a nearby organ is close and at risk of collateral heat damage.

Implementation of Real-time MPI-magnetic hyperthermia

An ideal real-time theranostic platform will allow real-time visualization of the pathology and the treatment region such that imaging is simultaneous with the therapy. Because the SPIONs also generate MPI signal during heating, real-time simultaneous MPI-therapy should be possible. To achieve this, the currently separate MPI imaging and MPI heating drive coils should be combined in one scanner with the addition of a receive coil optimized to pick up the MPI signal at f_0 = 354 kHz. Because the field-free-line needs to be constantly parked at a fixed location to maintain heat localization, one practical limitation is that the field-of-view is limited to the vicinity of the hyperthermia target location. However, this should not be a problem once the radiologist uses the initial MPI image to restrict the region-of-interest to the tumor vicinity.

If real-time imaging of a wider field-of-view is required, fast switching between imaging and heating modes could be designed such that heating is performed > 95% of the time and wide-view imaging in the other 5% (field-free-line is freed from its locked position to raster around). After the image, the FFL is immediately shifted back to focus heating on the desired spot again. This strategy is reasonable because MPI scans are relatively fast (3D

Lissajous trajectory at 46 frames per second[45]) and because movement of the SPIONs into and away from the tumor takes much longer than the time interval between imaging updates. For example, the enhanced permeability and retention wash-in and wash-out of SPIONs from the tumor as studied by MPI is shown to be on the time-scale of hours.[36]

Real-time Temperature Feedback with MPI Thermometry

Because assessment of thermal therapy and dosage is most accurate with *in vivo* temperature feedback, it is desirable to have some form of non-invasive measurement of the temperature of the treated site to act as feedback for a closed loop thermal therapy system. Optical temperature probes are limited to the skin surface, while IR cameras must deal with thermal background, depth attenuation and reflectance. MR thermometry,[20] while non-invasive and effective at depth, is difficult to implement in the vicinity of SPIONs because it is based on a 10 parts per billion per °C effect. SPIONs are known to induce larger variations in the MR signal than that.

In contrast, MPI thermometry benefits from the good attributes of MPI - being able to image at depth and having high sensitivity and contrast (no tissue signal). In essence, MPI thermometry uses the SPIONs as sensors of the *in vivo* microenvironment temperature. Prior work on *in vitro* MPI thermometry has been shown to be promising.[58,59] In brief, these methods rely on (1) using the SPIONs to measure the microenvironment viscosity which changes with temperature or (2) changes in the SPION magnetization response due to temperature dependence of the Langevin function for SPIONs. Using the latter method, MPI thermometry achieves a 0.4% change in the signal per °C.[58] This is more sensitive than MR thermometry (water signal changes by 10 parts per billion per °C).[20] Similar to the mode switching strategy of real-time MPI-magnetic hyperthermia, one can envision seamless fast switching from heating mode to temperature measurement mode. Because heating is expected to be slow, a temporal resolution of seconds to minutes should be acceptable. Furthermore, because only the temperature of the treatment region is of interest, time-consuming coverage of the entire field-of-view is not needed.

SAR and Magnetostimulation Safety Considerations

Time-varying magnetic fields can have two possible effects on the human body - (1) stimulation of nerves through induced electric fields, which often manifest as peripheral nerve stimulation, and (2) tissue heating *via* induced eddy currents in the body, which is measured by the specific absorption rate (SAR) metric. Because MPI and magnetic hyperthermia uses strong time-varying magnetic fields, the corresponding safety limits for these two effects are relevant.

From prior work, we note that below 42 kHz, safety is dominated by magnetostimulation limits while above 42 kHz, (induced eddy-current) SAR limits dominate.[26] Thus, the MPI imaging scan at 20 kHz has to address magnetostimulation. We note that while the 20 mT used in this work is safe for rodents, it is about 2-fold higher than the 8 mT limit for humans at 20 kHz.[26] To address this, MPI should use lower amplitudes of < 8 mT for clinical scans and this has been shown to be feasible and actually improve MPI performance especially in terms of spatial resolution.[60]

Next, the magnetic hyperthermia heating scan has to address SAR limits. While the 354 kHz and 13 mT used in this study is higher than the ~ 2 mT reported at 354 kHz, it must be noted that the reported values use a conservative SAR limit of 4 W/kg and a large torso radius of 20 cm. FDA SAR limits for localized heating of the torso is 10 W/kg.[61] Using 10W/kg and a 15 cm (average size) torso radius, and because SAR is proportional to $r^2 f^2 B_{pp}^2$, the limit is calculated to be 4.3 mT and is lower than the 13 mT used in this study.

One possible strategy to address SAR limits, depending on the particle, is to use a lower frequency but higher amplitude. In essence, one could further optimize and tailor the heating waveform to the nanoparticle characteristics. From the Rosensweig equation,[4]

$$P = \pi \mu_0 \chi_0 H^2 f \frac{2\pi f \tau}{1 + (2\pi f \tau)^2} \quad (1)$$

where τ is the relaxation time for reorientation of magnetic moments in SPION, we can see that while the heating power is strictly related to the square of the applied field amplitude H, increasing frequency f will always have less than an f^2 effect, with diminishing returns with larger τ. On the other hand, tissue SAR is proportional to $r^2 f^2 B_{pp}^2$,[62] therefore trading off frequency for amplitude does not change the SAR limit while heating gains may be observed from the Rosensweig equation if the frequency is too high for τ.

Another strategy is designing particles that heat more efficiently. This could help achieve the same *in vivo* heating and therapy reported in this work while lowering the required field amplitude to a safer level. For example, a very high nanoparticle SAR of 1019 W/g was reported for Zn-doped cubic SPIONs.[63] In addition, use of Exchange-coupling between a magnetically hard core ($CoFe_2O_4$) and soft shell ($MnFe_2O_4$) has enabled even higher SAR values of 3866 W/g at 100 kHz and 20 mT.[64] Recent work on ferromagnetic vortex-domain iron oxide has also shown similarly high SAR values.[65] These can be designed to be theranostic and usable for MRI (and potentially MPI) imaging as well as hyperthermia.[66,67] Using the Rosensweig equation (eqn. 1), we can back-calculate the field amplitude required to generate the same heating achieved in our results. With SAR values of 3.8 kW/g, the calculated value for field amplitude is much lower at around 2.6 mT and thus below the safe limit of 4.3 mT.

Lastly, because heating is most severe at the surface of the body due to the I^2 dependence (skin burns are most common), one possible way to mitigate risk from the 13 mT field is to cover the patient with a cooling surface to remove heat.

Path to Clinical Implementation

With high contrast and high sensitivity imaging, external control over the localization of therapy and the ability to work at any depth, MPI-magnetic hyperthermia can be a powerful image-guided therapy method for clinical cancer treatment. Preclinical MPI scanners are already commercially available and the barriers to clinical implementation are few and

addressable. The main challenge is maintaining high magnetic gradient strengths for large human-sized bores. We note that such gradients are already possible with current technology. For example, the gradient just outside a human 3.5 T MRI bore is approximately 7 T/m. The cost would thus be comparable to a clinical MRI scanner. If lower heating spatial precision is acceptable, lower gradients of 1 T/m could be used, removing the need for superconducting magnets and dramatically reducing the MPI scanner cost. This would make the MPI-magnetic hyperthermia procedure much more affordable.

Another key challenge is keeping within the clinical SPION dose limits while achieving sufficient concentration for heating. It was reported that 5mg/ml was a moderate concentration for clinical magnetic hyperthermia,[68] and another clinical magnetic hyperthermia pilot study, a prostate tissue SPION concentration of up to 30 mg/ml was reached during therapy.[69] Although concentrations of up to 75 mg/ml was injected in this study, quantitative imaging with MPI reveals that the *in vivo* concentration achieved is closer to ~ 30 mg/ml and is within the clinically relevant range. The net amount of iron injected into the tumor is 1.25 mg. Clinically, it is estimated that 0.25 – 1.0% of the total injected dose of nanoparticles reach the tumor.[18] Clinical doses of 510 mg Ferumoxytol was reported in prior work.[70] This shows that even with limited delivery efficiency to the tumor, 1.25 – 5 mg of NPs out of the 510 mg injected is expected to reach the tumor, therefore suggesting that 1.25 mg per tumor is clinically achievable. More importantly, these numbers underscore the importance of MPI spatial localization of magnetic hyperthermia in avoiding thermal damage to healthy tissues that received the remaining 99% of the injected dose.

With this clinically relevant dose, we demonstrate in this work that spatially localized temperature rise *in vivo* to > 43°C was achieved within 7 minutes, and in the presence of active blood perfusion, suggesting that MPI-magnetic hyperthermia is viable in humans. Lower doses can be used if the heating efficiency of the SPION is further improved and the heating excitation further optimized. Much lower dosage and concentrations could be used in MPI-magnetic hyperthermia applications where only mild hyperthermia therapy is desired (as an adjuvant or sensitization procedure for chemotherapy) or in applications where no macroscopic temperature change is required (*e.g.* drug delivery applications).

Conclusions

Here we have described the theoretical foundation, physical construction, and testing of an MPI-magnetic hyperthermia theranostic platform. We showed experimental data using MPI gradients to deliver targeted heating on demand to components of a phantom with an ability to selectively heat targets separated by as little as 7 mm with negligible heating of off-target sites. We have also showed *in vivo* experimental data using MPI image-guided localization of heat therapy in a rodent model with the use of MPI gradients for localization. We also showed the ability to sequentially target different locations *in vivo*, demonstrating arbitrary control of the heating spot. We demonstrated very good correlation of the MPI image intensity with the SAR deposited, proving that thermal dose planning can be easily performed *via* an MPI pre-scan. Through a luciferase assay and histological assessment, we verified that heat damage was indeed localized to the target tumor, while the off-target tumor or off-target healthy clearance organs, such as the liver, were spared. Together, these data

represent an important step towards the development of a MPI-magnetic hyperthermia theranostics platform. An important next step is to develop MPI thermometry for *in vivo* implementation in order to provide a temperature feedback mechanism for complete thermal dose control. Because achieving macroscopic heating with low amplitudes remains a challenge, another important direction is to explore MPI-magnetic hyperthermia for applications in targeted drug release by using the MPI gradient localization strategy to localize actuation of the drug-containing nanocarriers. Exploring other therapeutic approaches that do not require macroscopic temperature changes, such as activation of lysosomal pathways[71,72] and thermal drug delivery, are also of great interest.

Methods

Superparamagnetic Iron Oxide Nanoparticles (SPIONs)

SPION Synthesis—SPIONs were synthesized by the co-precipitation method optimized for high energy dissipation rates described by Mrida *et al.*[73]. Briefly, deionized water was degassed with nitrogen and used to prepare solutions of iron (II) chloride tetrahydrate (99%, Sigma-Aldrich) and iron (III) chloride hexahydrate (99%, Sigma-Aldrich) at a 1:2 molar ratio respectively, with a total iron concentration of 0.30 M. The iron salt solutions were sonicated, degassed, and mixed in a glass reactor. The reaction mixture was heated to 75°*C* and ammonium hydroxide (29% vol/vol, Fisher Scientific) was added to the mixture to raise pH to 8.0–9.0. The reaction temperature was increased to 85°*C* and allowed to react for one-hour. The pH was maintained around 8.0–9.0 by periodic addition of ammonium hydroxide. The resulting iron oxide nanoparticles were peptized using tetramethylammonium hydroxide (TMAOH, 1 M, Sigma-Aldrich) at a volume ratio 1:2 SPION/TMAOH twice. Peptized nanoparticles were suspended in water.

To coat the particles with polyethylene glycol (PEG), oleic acid (OA, 90%, Sigma-Aldrich) was adsorbed onto the particles. OA was added to SPIONs solution at 15 g OA/g SPIONs and ultrasonicated (Q700, Qsonica Sonicators) for 15 minutes. The mixture was transferred to a glass reactor, heated to 50°*C* and allowed to react for 2 hours. SPIONs were precipitated using twice the volume of ethanol (200 proof, Decon Labs) and magnetically decanted to recover the particles, following which they were suspended in toluene (> 98%, Sigma-Aldrich).

SPION Surface Modification with PEGsilane—PEGsilane was synthesized by a two-step process. First, mono-methoxy PEG (mPEG, 99.999%, Sigma-Aldrich) of 5 kDa molecular weight was converted to mPEG-COOH as described by Lele *et al.*[74] Briefly, 0.05 mol of mPEG suspended in 400 mL of acetone (99.8%, Fisher Chemicals), was oxidized by adding 16.1 mL of Jones reagent (solution of chromium trioxide in aqueous sulfuric acid) and allowed to react for 24 hours. The reaction was stopped by adding excess isopropanol (70%, Sigma-Aldrich), and impurities from the reaction removed with activated charcoal (12–40 mesh, ACROS Organics). Chromium salts and activated charcoal were removed through vacuum filtration, then the acetone solution was concentrated using a rotary evaporator. The mixture of mPEG-COOH was re-dissolved in 1M hydrochloric acid (37% w/v, Fisher Chemicals). Liquid-liquid extraction was performed using 75 mL of

dichloromethane (> 99.5%, Sigma-Aldrich) to extract the polymer to the organic phase. The solution was concentrated by rotary evaporation and the mPEG-COOH precipitated using cold ethyl ether (> 99.8%, Fisher Chemicals).

To obtain PEGsilane, amidation of mPEG-COOH with 3-aminopropyl triethoxysilane (APS, TCI America) was performed. Briefly, a 1:1 molar ratio of mPEG-COOH:APS was mixed together for 2 hours at 120°*C* and 500mbar. At the end, the PEGsilane was allowed to cool to room temperature and hardened. The SPIONs were coated with PEGsilane by ligand exchange, replacing the oleic acid molecules for PEGsilane, following a previously described procedure.[75] In brief, 3.5 g of PEGsilane dissolved in 250 mL of dry toluene was mixed with 250 mL of OA adsorbed SPIONs at 0.8 mg/mL, then 40 μL of acetic acid (99.8%, ACROS Organics) was added to catalyze the hydrolysis and condensation of the silane groups onto the SPION surface. The solution was placed in a shaker for 72 hours, after which PEGsilane coated SPIONs were precipitated using cold ethyl ether. The precipitate was dried and resuspended in water. SPIONs were then dialyzed to remove excess PEGsilane and further sterilized by filtration for animal experiments.

SPION Characterization—SPION's magnetic, physical, and hydrodynamic diameters were determined and the results shown in Fig. 11. Magnetic size distribution was determined using a Quantum Design Magnetic Property Measurement System 3 (MPMS3) Superconducting Quantum Inference Device (SQUID) magnetometer. Magnetization curves at room temperature were obtained for liquid samples in a PTFE sample holder with 100 μL of SPIONs suspended in water. Physical diameters were obtained using a Hitachi H 7000 Transmission Electron Microscope (TEM). Images of SPIONs at 1 mg/mL sampled on an Ultrathin Carbon Type A (3–4nm) with removable formvar grid from TedPella were acquired using a Veleta CCD side mount camera and were analyzed using ImageJ. Hydrodynamic diameters were determined through room temperature dynamic light scattering (DLS), using a particle size analyzer (Zeta PALS, Brookhaven Instruments). For DLS, aqueous nanoparticle samples (500 μL) with concentration between 0.1 and 1 mg/mL were filtered using a 0.2 μm syringe filter prior to measurements.

Dynamic Magnetization Response in Different Locations in the MPI Gradient—Experimental measurements of the magnitude of the gradient field was taken with a Lakeshore™475 DSP Gaussmeter (Lake Shore Cryotronics, Ohio, USA) and plotted in Fig. 4a. Subsequently, the 2D spatial localization of SAR was experimentally measured by shifting a point source tube to different positions in the gradient field. The normalized SAR value was calculated by taking the initial rate of temperature rise at each position and plotted in Fig. 4c. For Fig. 4b, simulations were performed to obtain the dynamic magnetization response of the SPIONs to an applied alternating field in the presence of a field gradient. The results was obtained from the numerical solution of the MRSh magnetization relaxation equation as outlined in.[76] The dynamic magnetization was normalized to the saturation magnetization to facilitate visualization and understanding of the effect of field gradient on the dynamic hysteresis loop. Here, the value of unity indicates that particles are in a state of saturation. The SPIONs synthesized by the co-precipitation method and coated with PEG typically form small clusters. Thus, assuming a two particle cluster containing particles of

diameter equal to 11.7 nm, an effective magnetic core diameter of 23.4 nm was used in the simulations. Interparticle interactions are not included in the model. The hydrodynamic diameter of the SPIONs was assumed to be approximately 40 nm as determined from DLS measurements. The suspension medium being water was assumed to have a viscosity of 0.89 mPa·s at 298 K. Simulations were executed using a bias field value corresponding to the magnitude of the gradient field measured at various positions (A, B, and C) in the setup. Excitation field frequency of 354 kHz and 13 mT amplitude was used to match the experimental conditions. Simulations were also executed at 100 kHz and 600 kHz excitation field frequencies to show that the strategy of localizing heat using a field gradient is flexible and also viable with a different setup.

Animal Procedures

Development of Tumor Xenograft—All animal procedures were approved by the Animal Care and Use Committee at UC Berkeley and conducted according to the National Research Council's Guide for the Care and Use of Laboratory Animals. Nude athymic mice between 7 – 9 weeks old (Charles River Laboratories) weighing approximately 23 g were used in this study. After one week habituation, tumor xenografts were developed by subcutaneous injection of 2 million cancer cells in 100μl of sterile 1× PBS into the flank. U87MG and MDA-MB-231-Luc cell lines were serum starved for four hours before use (UC Berkeley Cell Culture Facility). Tumor volumes in all mice were measured thrice a week using a vernier caliper. When the tumor volume reached approximately 100–150 mm^3, the mice were divided into control and experimental groups. For our controlled heating experiment a dual tumor model was developed in the same mice by implanting tumor cells subcutaneously in the shoulder and flank.

Animal Preparation for MPI-magnetic hyperthermia Procedure—MPI-magnetic hyperthermia experiments were carried out as outlined in Fig. 12. Experimental group 1 (n=5) and group 2 (n=4) with single U87MG xenografts received 1.25 mg Fe of SPION by intratumoral injection and 50 μl of 25 mg/ml SPION as a tail vein injection for a total of 2.5 mg Fe per mouse. All MPI/magnetic hyperthermia were carried out on murine models under anesthesia. The mice were maintained at 1–2% isoflurane (60–80 breaths-per minutes) mixed with medical oxygen (1 lpm) supplied *via* nose cone. The core body temperature was constantly monitored by an optical fiber thermal probe (Neoptix™) inserted into the rectum. The core body temperature was maintained at 36–37 °C before starting magnetic hyperthermia with the help of controlled warm air delivered into the imaging bore from an external heater. The systemically administered SPIONs were allowed to completely clear from circulation to the liver before MPI imaging and heating was performed (approximately 24 hours).

Experimental group 3 (n=3) and group 4 (n=1) with MDA-MB-231-Luc had two tumors per mouse, and each tumor received 1.25 mg Fe of SPION by intratumoral injection. Luciferase activity was measured after intraperitoneal injection of D-Luciferin Monosodium salt at a dose of 150 mg/kg reconstituted in 1× PBS (Pierce™ ThermoFisher Scientific). Bioluminescent signal were obtained using an IVIS Lumina system with auto exposure time and medium binning. The bioluminescent image were exported as DICOM and processed

off-line. The bioluminescent imaging was performed before and after the MPI-magnetic hyperthermia imaging and heating procedure.

Localization of heating *via* MPI gradients was performed in groups 1 and 3 while non-localized heating (where MPI gradients were turned off) was performed in groups 2 and 4. In experimental group 5 (n=2) with one dual U87MG tumor mouse and one dual MDA-MB-231-luc tumor mouse, each tumor received 1.25 mg Fe of SPION by intratumoral injection and sequential localized heating was performed by heating one tumor first then heating the other tumor to demonstrate arbitrary control of the heat localization within a single scan. For the control group (n=1, Control 1, sham) saline was injected intratumorally and had 50μl of 25 mg/ml SPION as a tail vein injection for a total of 1.25 mg Fe per mouse. Localized heating *via* MPI gradients was targeted at the (saline-injected) tumor to assess thermal resolution *via* measuring heating of the liver when targeting of a non-spio tumor was performed. Control 2 (n=1) received both an intratumor and tail vein injection of saline (volumes and procedure same as Experimental Group 1) and non-localized heating was performed to assess nonspecific tissue-based SAR from the 354 kHz 13 mT magnetic field. Control 3 (n=1) received both an intratumor and tail vein injection of SPIONs (volumes and concentration same as Experimental Group 1) but received no heating from magnetic fields. After treatment with magnetic hyperthermia, all mice were observed for signs of superficial skin burns, signs of distress and discomfort, hunched posture, respiratory difficulties, or reticence to move. The hyperthermia procedure was immediately terminated if the core body temperature reached 40°C in accordance with prior literature on the response of mice to changes in their core body temperature[77] as well as prior work on minimal thermal damage thresholds required to cause damage to tissue.[56,57]

Histological Assessment—Animals in group 2, 4 and 5 were euthanized 2 hours after hyperthermia treatment (kept under isoflurane) while animals in group 1 and 3 were monitored for up to 3 days post treatment before euthanasia. Animals were first put under isoflurane anesthesia, then euthanized by carbon dioxide asphyxiation and cervical dislocation. After euthanasia, the tumor, liver, spleen and muscle surrounding the tumor was immediately excised and preserved in 10% formalin as preparation for histological sectioning. Hematoxylin and eosin (H & E) staining was done to assess tissue damage and Prussian Blue staining was done to assess SPION distribution within the tissue. *In Situ* Cell Death Detection Kit (TUNEL stain, TMR Red, Roche Diagnostics GmbH, Mannheim Germany) with nucleus counter-stained with DAPI was used to assess for apoptotic cells resulting from thermal damage. The slides were observed using appropriate color filters (ZEISS AX10 Observer D1 with a ZEISS Axiocam ERc 5s). FIJI software and its standard cell counting algorithm[78,79] was used in calculating the percentage of cells that underwent apoptosis.

Imaging and Magnetic Hyperthermia

After administration of the SPIONs, the mice were imaged in the custom-built Berkeley 3D MPI scanner described in prior work.[37] The 3D MPI scanner has a 6.3 T/m MPI gradient generated by water-cooled electromagnets with a field-free-line configuration and has a drive field at 20.25 kHz and 20 mT amplitude. The field-free-line was rastered through the

field-of-view of 12.35 cm × 4.75 cm × 4.75 cm and 2D projection images were acquired. The scan time was approximately 2 minutes excluding robot arm motion time. The FFL with axis along the y-direction was electromagnetically shifted along the x-axis as shown in Fig. 2. The animal bed was mechanically translated by a robot arm in the z-direction at 1 mm increments to complete projection imaging of the x-z plane. All images were reconstructed using x-space MPI reconstruction algorithm described in prior work.[37] To obtain a 3D volume, the field-free-line was taken at different angles through the mice and the 3D volume is reconstructed with projection recon algorithms as described in our prior work on MPI tomography.[80] To provide an anatomic reference, projection X-ray was taken after the MPI scan when the mice were alive and at the end of treatment, a post-mortem CT was taken to provide a 3D anatomic reference.

After an MPI image is obtained of the biodistribution of the SPIONs within the mice, localized heating of the SPIONs was performed at a 2.35 T/m gradient with field-free-line configuration created with NdFeB permanent magnets and a drive field of 354 kHz and 13 mT. The heating duration is between 30 minutes – 60 minutes depending on the real-time *in vivo* temperature measurements from which real-time updates on the total thermal dose could be obtained in order to achieve CEM43 of ~ 60 – 90 minutes. The equation[55] for CEM43 used is :

$$\mathrm{CEM43} = \sum_{i=1}^{n} t_i \cdot R^{(43 - T_i)} \quad (2)$$

where R is 0.5 when above 43°C and R is 0.25 when below 43°C.

To perform image-guided localization of heating, the home field-free-line coordinates of both scans were aligned. From the obtained MPI image, the required displacement of the field-free-line from the home position to the desired target location was calculated. This value is used by the robot arm to shift the animal bed relative to the field-free-line. This is to align the field-free-line to the *in vivo* target location in order to localize the heating to the desired location. A detailed pictorial representation of the hardware used and the image-guidance workflow is presented in Fig. 2.

***In Vivo* Temperature Measurement—**Neoptix™fiber optic temperature sensors were placed on the surface of the flank tumor and inserted into the intraperitoneal cavity and placed close to the liver to obtain real-time tumor and liver temperature measurements. One sensor was inserted into the rectum to measure the core body temperature as typically performed in prior hyperthermia studies.[38] The fiber optic probes interfaced with the Neoptix Reflex™that has a measurement accuracy of ±0.8°C and sampling rate of approximately 1 sample per second.

Heating Localization Characterization—For Fig. 4c, the experimental set-up used a nanoparticle point source located on the Neoptix probe tip (5 μL held in position by a narrow capillary sheath) was moved by small distances (0.5 mm per step in the x-z plane) by a robot arm and initial heating rate in response to a 354 kHz 13 mT excitation was measured at each

location in the MPI gradient field to calculate the SAR. This is because SAR for an object at thermal equilibrium with the surroundings is proportional to the instantaneous initial temperature rise. The point source was allowed to cool then moved to a new position and heated again to form a 2D SAR image of the effect of the MPI gradient field on heating.

MPI Characterization—The experimental setup for Fig. 7a. involves an in vitro dilution series of the SPIONs in 9 separate capillary tubes (2 microliter volume each) that are then imaged individually in the Berkeley MPI imaging scanner described in Fig. 12. The range of SPION concentrations used are from 7.5 mg/ml to 0.03 mg/ml and net mass of SPION per tube is thus known. For Fig. 7b., we first performed an MPI scan on the mice and the MPI signal intensity at the tumor measured. Subsequently, the mice underwent magnetic hyperthermia with the heating target located at the tumor, and the local temperature rise was measured using the NeoptixTM fiber probes. Specific Absorption Rate (SAR) was calculated from the initial temperature rise dT/dt using the equation $SAR = dT/dt \cdot C_p \cdot V \cdot \rho \div (mass_{Fe} \cdot 1000)$. Mass of Fe is proportional to *in vivo* MPI signal and calculated from the proportional constant of 0.43 a.u. per mg Fe measured from Fig. 7a. For Fig. 7c., the local SAR was calculated in the same way as Fig. 7b. by measuring the temperature rise at different tumors. The heating targeting and MPI gradient conditions are specified in the figure. The local SAR values reported in Fig. 7c. are normalized to SAR per mg of Fe in the tumor.

Predictive Algorithm for Thermal Dose Planning—Because MPI is quantitative for the mass of SPION, and since SAR is proportional to the SPION mass, we can obtain a SAR image from the MPI image. To predict the localization effect of the MPI gradients, we dot multiply the SAR image with suppression effect of the MPI gradient which is in essence a SAR spatial filter. We thus obtain a prediction of the SAR dose after gradient localization. Finally, to account for heat spreading through tissue from the SPION mass, we convolve the previous image with a temperature spatial point spread function (PSF).

To measure the SAR suppression effect of the MPI gradient, we measured the temperature rise (Neoptix™probe) of a point source of SPIONs (1.4 mm ID tube, 354 kHz, 13 mT excitation) as it is moved to different positions (x-z plane) in the background gradient field. To measure the temperature spatial point spread function (PSF), we created a 2 mm ID well in an 2% agarose gel phantom and filled it with 50μl of 25 mg/ml SPIONs. Constant heating was performed at 354 kHz, 13 mT and temperature of the agarose at various distances from the central well was measured (Neoptix™probe). When the temperature reaches steady-state, the spatial temperature profile of the agarose was recorded.

Acknowledgments

We gratefully acknowledge support from NIH grants R01 EB019458 and EB024578, UC TRDRP grant 26IP-0049, M. Cook Chair and the UC Discovery Award. Additionally, work at the University of Florida was supported by NIH 1R21 EB018453-01A1 and the University of Florida Health Cancer Center. We would also like to acknowledge NIH grants 1R43 DA041814-01A1, 5R43 EB020463-02 and fellowship support from the Siebel Scholars Foundation and the Agency of Science Technology and Research, Singapore (Z. Tay).

References

1. Hensley DW, Tay ZW, Dhavalikar R, Zheng B, Goodwill P, Rinaldi C, Conolly S. Combining Magnetic Particle Imaging and Magnetic Fluid Hyperthermia in a Theranostic Platform. Phys Med Biol. 2016; 62:3483–3501. [PubMed: 28032621]
2. Rodrigues HF, Capistrano G, Mello FM, Zufelato N, Silveira-Lacerda E, Bakuzis AF. Precise Determination of the Heat Delivery during In Vivo Magnetic Nanoparticle Hyperthermia with Infrared Thermography. Phys Med Biol. 2017; 62:4062–4082. [PubMed: 28306552]
3. Jordan A, Scholz R, Wust P, Fähling H, Felix R. Magnetic Fluid Hyperthermia (MFH): Cancer Treatment with AC Magnetic Field Induced Excitation of Biocompatible Superparamagnetic Nanoparticles. J Magn Magn Mater. 1999; 201:413–419.
4. Rosensweig RE. Heating Magnetic Fluid with Alternating Magnetic Field. J Magn Magn Mater. 2002; 252:370–374.
5. Jordan A, Scholz R, Maier-Hauff K, van Landeghem FK, Waldoefner N, Teichgraeber U, Pinkernelle J, Bruhn H, Neumann F, Thiesen B, Von Diemling A, Felix R. The Effect of Thermotherapy Using Magnetic Nanoparticles on Rat Malignant Glioma. J Neuro-Oncol. 2006; 78:7–14.
6. Thiesen B, Jordan A. Clinical Applications of Magnetic Nanoparticles for Hyperthermia. Int J Hyperthermia. 2008; 24:467–474. [PubMed: 18608593]
7. Weissleder R, Stark DD, Engelstad BL, Bacon BR, Compton CC, White DL, Jacobs P, Lewis J. Superparamagnetic Iron Oxide: Pharmacokinetics and Toxicity. AJR Am J Roentgenol. 1989; 152:167–173. [PubMed: 2783272]
8. Pouliquen D, Le Jeune JJ, Perdrisot R, Ermias A, Jallet P. Iron Oxide Nanoparticles for Use as an MRI Contrast Agent: Pharmacokinetics and Metabolism. Magn Reson Imaging. 1991; 9:275–283. [PubMed: 1881245]
9. Alvarez-Berrios MP, Castillo A, Merida F, Mendez J, Rinaldi C, Torres-Lugo M. Enhanced Proteotoxic Stress: One of the Contributors for Hyperthermic Potentiation of the Proteasome Inhibitor Bortezomib using Magnetic Nanoparticles. Biomater Sci. 2015; 3:391–400. [PubMed: 26218130]
10. Alvarez-Berríos MP, Castillo A, Rinaldi C, Torres-Lugo M. Magnetic Fluid Hyperthermia Enhances Cytotoxicity of Bortezomib in Sensitive and Resistant Cancer Cell Lines. Int J Nanomedicine. 2014; 9:145–153.
11. Alvarez-Berríos MP, Castillo A, Mendéz J, Soto O, Rinaldi C, Torres-Lugo M. Hyperthermic Potentiation of Cisplatin by Magnetic Nanoparticle Heaters is Correlated with an Increase in Cell Membrane Fluidity. Int J Nanomedicine. 2013; 8:1003–1013. [PubMed: 23493492]
12. Lee JS, Rodríguez-Luccioni HL, Méndez J, Sood AK, Lpez-Berestein G, Rinaldi C, Torres-Lugo M. Hyperthermia Induced by Magnetic Nanoparticles Improves the Effectiveness of the Anticancer Drug Cis-diamminedichloroplatinum. J Nanosci Nanotechnol. 2011; 11:4153–4157. [PubMed: 21780419]
13. Torres-Lugo M, Rinaldi C. Thermal Potentiation of Chemotherapy by Magnetic Nanoparticles. Nanomedicine. 2013; 8:1689–1707. [PubMed: 24074390]
14. Ito A, Honda H, Kobayashi T. Cancer Immunotherapy based on Intracellular Hyperthermia using Magnetite Nanoparticles: a Novel Concept of “Heat-Controlled Necrosis” with Heat Shock Protein Expression. Cancer Immunol Immunother. 2006; 55:320–328. [PubMed: 16133113]
15. Toraya-Brown S, Sheen MR, Zhang P, Chen L, Baird JR, Demidenko E, Turk MJ, Hoopes PJ, Conejo-Garcia JR, Fiering S. Local Hyperthermia Treatment of Tumors Induces CD8(+) T Cell-mediated Resistance Against Distal and Secondary Tumors. Nanomedicine. 2014; 10:1273–1285. [PubMed: 24566274]
16. Jordan A, Scholz R, Maier-Hauff K, Johannsen M, Wust P, Nadobny J, Schirra H, Schmidt H, Deger S, Loening S, Lanksch W, Felix R. Presentation of a New Magnetic Field Therapy System for the Treatment of Human Solid Tumors with Magnetic Fluid Hyperthermia. J Magn Magn Mater. 2001; 225:118–126.
17. Kut C, Zhang Y, Hedayati M, Zhou H, Cornejo C, Bordelon D, Mihalic J, Wabler M, Burghardt E, Gruettner C, Geyh A, Brayton C, Deweese TL, Ivkov R. Preliminary Study of Injury from Heating

Systemically Delivered, Nontargeted Dextran-Superparamagnetic Iron Oxide Nanoparticles in Mice. Nanomedicine. 2012; 7:1697–1711. [PubMed: 22830502]

18. Wilhelm S, Tavares AJ, Dai Q, Ohta S, Audet J, Dvorak HF, Chan WCW. Analysis of Nanoparticle Delivery to Tumours. Nat Rev Mater. 2016; 1:16014–16014.
19. Hensley D, Tay ZW, Dhavalikar R, Goodwill P, Zheng B, Rinaldi C, Conolly S. A Theranostic Platform for Localized Magnetic Fluid Hyperthermia and Magnetic Particle Imaging. Proc SPIE. 2017:1006603–1006601.
20. Rieke V, Butts Pauly K. MR Thermometry. J Magn Reson Imaging. 2008; 27:376–390. [PubMed: 18219673]
21. Gleich B, Weizenecker J. Tomographic Imaging Using the Nonlinear Response of Magnetic Particles. Nature. 2005; 435:1214–1217. [PubMed: 15988521]
22. Knopp T, Biederer S, Sattel TF, Erbe M, Buzug TM. Prediction of the Spatial Resolution of Magnetic Particle Imaging using the Modulation Transfer Function of the Imaging Process. IEEE Trans Med Imaging. 2011; 30:1284–1292. [PubMed: 21317081]
23. Rahmer J, Weizenecker J, Gleich B, Borgert J. Signal Encoding in Magnetic Particle Imaging: Properties of the System Function. BMC Med Imaging. 2009; 9:4–4. [PubMed: 19335923]
24. Franke J, Heinen U, Lehr H, Weber A, Jaspard F, Ruhm W, Heidenreich M, Schulz V. System Characterization of a Highly Integrated Preclinical Hybrid MPI-MRI Scanner. IEEE Trans Med Imaging. 2016; 35:1993–2004. [PubMed: 26991821]
25. Vogel P, Ruckert MA, Klauer P, Kullmann WH, Jakob PM, Behr VC. Superspeed Traveling Wave Magnetic Particle Imaging. IEEE Trans Magn. 2015; 51:1–3. [PubMed: 26203196]
26. Saritas EU, Goodwill PW, Croft LR, Konkle JJ, Lu K, Zheng B, Conolly SM. Magnetic Particle Imaging (MPI) for NMR and MRI Researchers. J Magn Reson. 2013; 229:116–126. [PubMed: 23305842]
27. Goodwill PW, Conolly SM. The X-Space Formulation of the Magnetic Particle Imaging Process: 1-D Signal, Resolution, Bandwidth, SNR, SAR, and Magnetostimulation. IEEE Trans Med Imaging. 2010; 29:1851–1859. [PubMed: 20529726]
28. Saritas EU, Goodwill PW, Zhang GZ, Conolly SM. Magnetostimulation Limits in Magnetic Particle Imaging. IEEE Trans Med Imaging. 2013; 32:1600–1610. [PubMed: 23649181]
29. Haegele J, Rahmer J, Gleich B, Borgert J, Wojtczyk H, Panagiotopoulos N, Buzug TM, Barkhausen J, Vogt FM. Magnetic particle imaging: visualization of instruments for cardiovascular intervention. Radiology. 2012; 265:933–938. [PubMed: 22996744]
30. Zheng B, Vazin T, Goodwill P, Conway A, Verma A, Saritas E, Schaffer D, Conolly S. Magnetic Particle Imaging Tracks the Long-term Fate of In Vivo Neural Cell Implants with High Image Contrast. Sci Rep. 2015; 5:14055. [PubMed: 26358296]
31. Zheng B, von See MP, Yu E, Gunel B, Lu K, Vazin T, Schaffer DV, Goodwill PW, Conolly SM. Quantitative Magnetic Particle Imaging Monitors the Transplantation, Biodistribution, and Clearance of Stem Cells In Vivo. Theranostics. 2016; 6:291–301. [PubMed: 26909106]
32. Fidler F, Steinke M, Kraupner A, Gruttner C, Hiller KH, Briel A, Westphal F, Walles H, Jakob PM. Stem Cell Vitality Assessment Using Magnetic Particle Spectroscopy. IEEE Trans Magn. 2015; 51:1–4. [PubMed: 26203196]
33. Orendorff R, Wendland M, Yu E, Zheng B, Goodwill P, Conolly S. First in vivo Brain Perfusion Imaging using Magnetic Particle Imaging. 2016 World Molecular Imaging Congress (WMIC 2016): Imaging Biology Improving Therapy. 2016
34. Zhou XY, Jeffris K, Yu E, Zheng B, Goodwill P, Nahid P, Conolly S. First *in vivo* Magnetic Particle Imaging of Lung Perfusion in Rats. Phys Med Biol. 2017:3510–3522. [PubMed: 28218614]
35. Nishimoto K, Mimura A, Aoki M, Banura N, Murase K. Application of Magnetic Particle Imaging to Pulmonary Imaging Using Nebulized Magnetic Nanoparticles. Open J Med Imaging. 2015; 5:49.
36. Yu EY, Bishop M, Zheng B, Ferguson RM, Khandhar AP, Kemp SJ, Krishnan KM, Goodwill PW, Conolly SM. Magnetic Particle Imaging: A Novel in vivo Imaging Platform for Cancer Detection. Nano Lett. 2017; 17:1648–1654. [PubMed: 28206771]

37. Yu EY, Chandrasekharan P, Berzon R, Tay ZW, Zhou XY, Khandhar AP, Ferguson RM, Kemp SJ, Zheng B, Goodwill PW, Wendland MF, Krishnan KM, Behr S, Carter J, Conolly SM. Magnetic Particle Imaging for Highly Sensitive, Quantitative, and Safe in Vivo Gut Bleed Detection in a Murine Model. ACS Nano. 2017; 11:12067–12076. [PubMed: 29165995]
38. Murase K, Aoki M, Banura N, Nishimoto K, Mimura A, Kuboyabu T, Yabata I. Usefulness of Magnetic Particle Imaging for Predicting the Therapeutic Effect of Magnetic Hyperthermia. Open J Med Imaging. 2015; 5:85–99.
39. Banura N, Mimura A, Nishimoto K, Murase K. Heat Transfer Simulation for Optimization and Treatment Planning of Magnetic Hyperthermia Using Magnetic Particle Imaging. arXiv. 2016; 1605:8139–8139.
40. Graeser M, Knopp T, Szwargulski P, Friedrich T, von Gladiss A, Kaul M, Krishnan KM, Ittrich H, Adam G, Buzug TM. Towards Picogram Detection of Superparamagnetic Iron-Oxide Particles Using a Gradiometric Receive Coil. Sci Rep. 2017; 7:6872. [PubMed: 28761103]
41. Them K, Salamon J, Szwargulski P, Sequeira S, Kaul MG, Lange C, Ittrich H, Knopp T. Increasing the Sensitivity for Stem Cell Monitoring in System-function Based Magnetic Particle Imaging. Phys Med Biol. 2016; 61:3279–3290. [PubMed: 27032447]
42. Them K, Kaul MG, Jung C, Hofmann M, Mummert T, Werner F, Knopp T. Sensitivity Enhancement in Magnetic Particle Imaging by Background Subtraction. IEEE Trans Med Imaging. 2016; 35:893–900. [PubMed: 26599700]
43. Salamon J, Hofmann M, Jung C, Kaul MG, Werner F, Them K, Reimer R, Nielsen P, Vom Scheidt A, Adam G, Knopp T, Ittrich H. Magnetic Particle/Magnetic Resonance Imaging: In-Vitro MPI-Guided Real Time Catheter Tracking and 4D Angioplasty Using a Road Map and Blood Pool Tracer Approach. PLoS One. 2016; 11:e0156899. [PubMed: 27249022]
44. Rahmer J, Wirtz D, Bontus C, Borgert J, Gleich B. Interactive Magnetic Catheter Steering with 3D Real-Time Feedback Using Multi-Color Magnetic Particle Imaging. IEEE Trans Med Imaging. 2017; 36:1449–1456. [PubMed: 28287965]
45. Ludewig P, Gdaniec N, Sedlacik J, Forkert ND, Szwargulski P, Graeser M, Adam G, Kaul MG, Krishnan KM, Ferguson RM, Khandhar AP, Walczak P, Fiehler J, Thomalla G, Gerloff C, Knopp T, Magnus T. Magnetic Particle Imaging for Real-Time Perfusion Imaging in Acute Stroke. ACS Nano. 2017; 11:10480–10488. [PubMed: 28976180]
46. Tay ZW, Goodwill PW, Hensley DW, Taylor LA, Zheng B, Conolly SM. A High-Throughput, Arbitrary-Waveform, MPI Spectrometer and Relaxometer for Comprehensive Magnetic Particle Optimization and Characterization. Sci Rep. 2016; 6:34180. [PubMed: 27686629]
47. Rahmer J, Halkola A, Gleich B, Schmale I, Borgert J. First Experimental Evidence of the Feasibility of Multi-color Magnetic Particle Imaging. Phys Med Biol. 2015; 60:1775–1791. [PubMed: 25658130]
48. Goodwill PW, Lu K, Zheng B, Conolly SM. An X-Space Magnetic Particle Imaging Scanner. Rev Sci Instrum. 2012; 83:033708. [PubMed: 22462930]
49. Goodwill PW, Konkle JJ, Zheng B, Saritas EU, Conolly SM. Projection X-Space Magnetic Particle Imaging. IEEE Trans Med Imaging. 2012; 31:1076–1085. [PubMed: 22552332]
50. Dhavalikar R, Rinaldi C. Theoretical Predictions for Spatially-Focused Heating of Magnetic Nanoparticles Guided by Magnetic Particle Imaging Field Gradients. J Magn Magn Mater. 2016; 419:267–273. [PubMed: 28943706]
51. Tay ZW, Hensley D, Vreeland E, Zheng B, Conolly S. The Relaxation Wall: Experimental Limits to Improving MPI Spatial Resolution by Increasing Nanoparticle Core Size. Biomed Phys Eng Express. 2017; 3:035003. [PubMed: 29250434]
52. Yu, EY., Goodwill, PW., Conolly, SM. Preliminary Characterization of a Laminated Iron-Core 6.3 T/m FFL magnet. Magnetic Particle Imaging (IWMPI), 2015 5th International Workshop on; 2015; p. 1-1.
53. Tasci TO, Vargel I, Arat A, Guzel E, Korkusuz P, Atalar E. Focused RF Hyperthermia using Magnetic Fluids. Med Phys. 2009; 36:1906–1912. [PubMed: 19544810]
54. King MA, Leon LR, Mustico DL, Haines JM, Clanton TL. Biomarkers of Multiorgan Injury in a Preclinical Model of Exertional Heat Stroke. J Appl Physiol. 2015; 118:1207–1220. [PubMed: 25814640]

55. van Rhoon GC, Samaras T, Yarmolenko PS, Dewhirst MW, Neufeld E, Kuster N. CEM43C Thermal Dose Thresholds: a Potential Guide for Magnetic Resonance Radiofrequency Exposure Levels? Eur Radiol. 2013; 23:2215–2227. [PubMed: 23553588]
56. van Rhoon GC. Is CEM43 Still a Relevant Thermal Dose Parameter for Hyperthermia Treatment Monitoring? Int J Hyperthermia. 2016; 32:50–62. [PubMed: 26758036]
57. Yarmolenko PS, Moon EJ, Landon C, Manzoor A, Hochman DW, Viglianti BL, Dewhirst MW. Thresholds for Thermal Damage to Normal Tissues: an Update. Int J Hyperthermia. 2011; 27:320–343. [PubMed: 21591897]
58. Weaver JB, Rauwerdink AM, Hansen EW. Magnetic Nanoparticle Temperature Estimation. Med Phys. 2009; 36:1822–1829. [PubMed: 19544801]
59. Perreard IM, Reeves DB, Zhang X, Kuehlert E, Forauer ER, Weaver JB. Temperature of the Magnetic Nanoparticle Microenvironment: Estimation from Relaxation Times. Phys Med Biol. 2014; 59:1109–1119. [PubMed: 24556943]
60. Croft LR, Goodwill PW, Konkle JJ, Arami H, Price DA, Li AX, Saritas EU, Conolly SM. Low Drive Field Amplitude for Improved Image Resolution in Magnetic Particle Imaging. Med Phys. 2016; 43:424–435. [PubMed: 26745935]
61. Zaremba, L. Magnetic Resonance Procedures: Health Effects and Safety, Special Edition. Shellock, F., editor. CRC Press; Boca Raton: 2001. p. 183-196.
62. Brown RW, Cheng Y-CN, Mark Haacke E, Thompson MR, Venkatesan R. Magnetic Resonance Imaging : Physical Principles and Sequence Design (2). 2014; 1:1.
63. Bauer LM, Situ SF, Griswold MA, Samia ACS. High-Performance Iron Oxide Nanoparticles for Magnetic Particle Imaging–Guided Hyperthermia (hMPI). Nanoscale. 2016:12162–12169. [PubMed: 27210742]
64. Lee JH, Jang JT, Choi JS, Moon SH, Noh SH, Kim JW, Kim JG, Kim IS, Park KI, Cheon J. Exchange-coupled magnetic nanoparticles for efficient heat induction. Nat Nanotechnol. 2011; 6:418. [PubMed: 21706024]
65. Liu XL, Yang Y, Ng CT, Zhao LY, Zhang Y, Bay BH, Fan HM, Ding J. Magnetic vortex nanorings: a new class of hyperthermia agent for highly efficient in vivo regression of tumors. Adv Mater. 2015; 27:1939–1944. [PubMed: 25655680]
66. Liu XL, Ng CT, Chandrasekharan P, Yang HT, Zhao LY, Peng E, Lv YB, Xiao W, Fang J, Yi JB, Zhang H, Chuang KH, Bay BH, Ding J, Fan HM. Synthesis of Ferromagnetic Fe0.6 Mn0.4 O Nanoflowers as a New Class of Magnetic Theranostic Platform for In Vivo T1 -T2 Dual-Mode Magnetic Resonance Imaging and Magnetic Hyperthermia Therapy. Adv Healthcare Mater. 2016; 5:2092–2104.
67. Chandrasekharan P, Maity D, Yong CX, Chuang KH, Ding J, Feng SS. Vitamin E (D-alpha-tocopheryl-co-poly(ethylene glycol) 1000 succinate) micelles-superparamagnetic iron oxide nanoparticles for enhanced thermotherapy and MRI. Biomaterials. 2011; 32:5663–5672. [PubMed: 21550654]
68. Jordan A, Wust P, Fähling H, John W, Hinz A, Felix R. Inductive Heating of Ferrimagnetic Particles and Magnetic Fluids: Physical Evaluation of their Potential for Hyperthermia. Int J Hyperthermia. 2009; 25:499–511. [PubMed: 19848612]
69. Johannsen M, Gneveckow U, Eckelt L, Feussner A, Waldöfner N, Scholz R, Deger S, Wust P, Loening S, Jordan A. Clinical Hyperthermia of Prostate Cancer using Magnetic Nanoparticles: Presentation of a New Interstitial Technique. Int J Hyperthermia. 2005; 21:637–647. [PubMed: 16304715]
70. Lu M, Cohen MH, Rieves D, Pazdur R. FDA report: Ferumoxytol for Intravenous Iron Therapy in Adult Patients with Chronic Kidney Disease. Am J Hematol. 2010; 85:315–319. [PubMed: 20201089]
71. Domenech M, Marrero-Berrios I, Torres-Lugo M, Rinaldi C. Lysosomal Membrane Permeabilization by Targeted Magnetic Nanoparticles in Alternating Magnetic Fields. ACS Nano. 2013; 7:5091–5101. [PubMed: 23705969]
72. Creixell M, Bohorquez AC, Torres-Lugo M, Rinaldi C. EGFR-Targeted Magnetic Nanoparticle Heaters Kill Cancer Cells without a Perceptible Temperature Rise. ACS Nano. 2011; 5:7124–7129. [PubMed: 21838221]

73. Mérida F, Chiu-Lam A, Bohórquez AC, Maldonado-Camargo L, Pérez ME, Pericchi L, Torres-Lugo M, Rinaldi C. Optimization of Synthesis and Peptization Steps to Obtain Iron Oxide Nanoparticles with High Energy Dissipation Rates. J Magn Magn Mater. 2015; 394:361–371. [PubMed: 26273124]

74. Lele BS, Kulkarni MG. Single Step Room Temperature Oxidation of Poly (ethylene glycol) to Poly(oxyethylene)-dicarboxylic Acid. J Appl Polym Sci. 1998; 70:883–890.

75. Barrera C, Herrera AP, Rinaldi C. Colloidal Dispersions of Monodisperse Magnetite Nanoparticles Modified with Poly(ethylene glycol). J Colloid Interface Sci. 2009; 329:107–113. [PubMed: 18930466]

76. Dhavalikar R, Hensley D, Maldonado-Camargo L, Croft LR, Ceron S, Goodwill PW, Conolly SM, Rinaldi C. Finite Magnetic Relaxation in X-Space Magnetic Particle Imaging: Comparison of Measurements and Ferrohydrodynamic Models. J Phys D Appl Phys. 2016; 49:305002. [PubMed: 27867219]

77. Duhan V, Joshi N, Nagarajan P, Upadhyay P. Protocol for Long Duration Whole Body Hyperthermia in Mice. J Vis Exp. 2012:e3801. [PubMed: 22951580]

78. Rueden CT, Schindelin J, Hiner MC, DeZonia BE, Walter AE, Arena ET, Eliceiri KW. ImageJ2: ImageJ For The Next Generation of Scientific Image Data. BMC Bioinformatics. 2017; 18:529. [PubMed: 29187165]

79. Schindelin J, Arganda-Carreras I, Frise E, Kaynig V, Longair M, Pietzsch T, Preibisch S, Rueden C, Saalfeld S, Schmid B, Tinevez JY, White DJ, Hartenstein V, Eliceiri K, Tomancak P, Cardona A. Fiji: An Open-Source Platform for Biological-Image Analysis. Nat Methods. 2012; 9:676–682. [PubMed: 22743772]

80. Konkle JJ, Goodwill PW, Carrasco-Zevallos OM, Conolly SM. Projection Reconstruction Magnetic Particle Imaging. IEEE Trans Med Imaging. 2013; 32:338–347. [PubMed: 23193308]

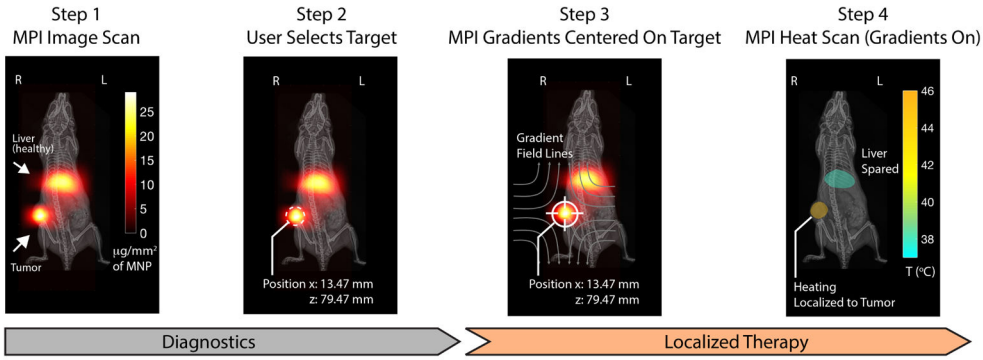

Figure 1.

TheranosticWorkflow demonstrated experimentally on a U87MG xenograft mouse model with Superparamagnetic Iron Oxide Nanoparticles (SPIONs) present in the liver and tumor. Step 1: an Magnetic Particle Imaging (MPI) image scan at 20 kHz, 20 mT enables clear visualization with high contrast of the SPION biodistribution in regions of pathology (tumor) and also in healthy clearance organs (liver). Imaging parameters are such that SPIONs do not heat. Step 2: the user selects a region, in this case the tumor, to localize the magnetic hyperthermia to. Step 3: The MPI gradients are shifted to center the field-free region (FFR) on the target. This magnetically saturates SPIONs away from the FFR to prevent heating. Step 4: Heat scan at 354 kHz, 13 mT is performed while the MPI gradients are on and held in position. Heating is experimentally localized in the FFR (centered at tumor) while minimizing collateral heat damage to the liver.

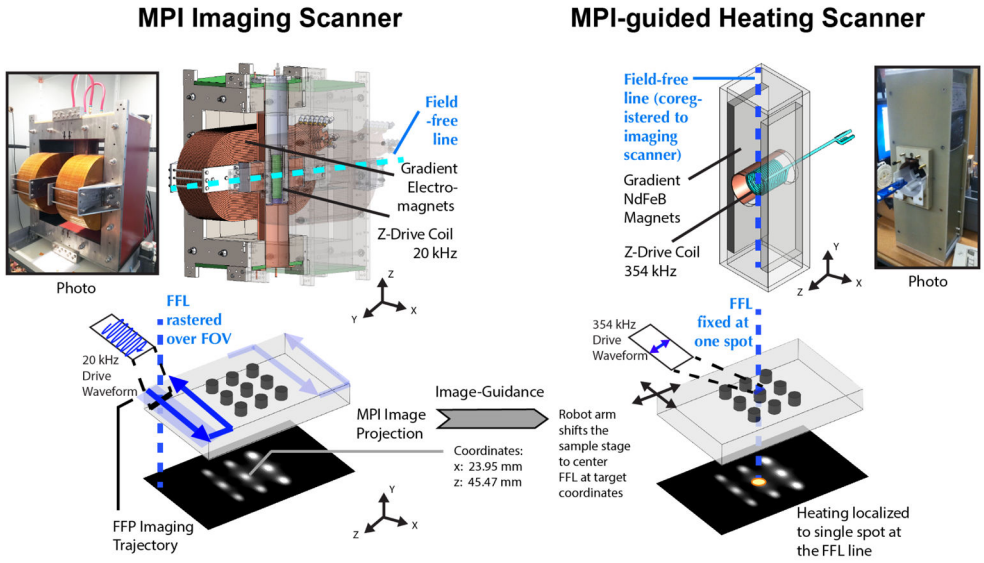

Figure 2.

Hardware setup of the MPI scanner and the image-guided magnetic hyperthermia scanner. Images are first obtained on our Berkeley MPI Scanner (validated in prior work[37]). To obtain an image, the sensitive field-free-region (FFR) is rastered through a volume. In this study, a field-free-line geometry is used, and images obtained are similar to projection scintigraphy. A separate higher-frequency MPI scanner is used for application of magnetic hyperthermia but has the same geometry, field-free-line. The coordinates are matched to the coordinates of the field-free-line (FFL) of the imaging scanner so as to enable image-guidance from the first scanner. The user is able to pick a target from the image, and the corresponding coordinates on the image is sent to the MPI heating scanner. The robot arm shifts the co-registered animal bed to center the FFL of the heating scanner to the requested coordinates. To locally heat only the target spot, the field-free-line is held in place over the spot while a higher frequency (354kHz) excitation is performed.

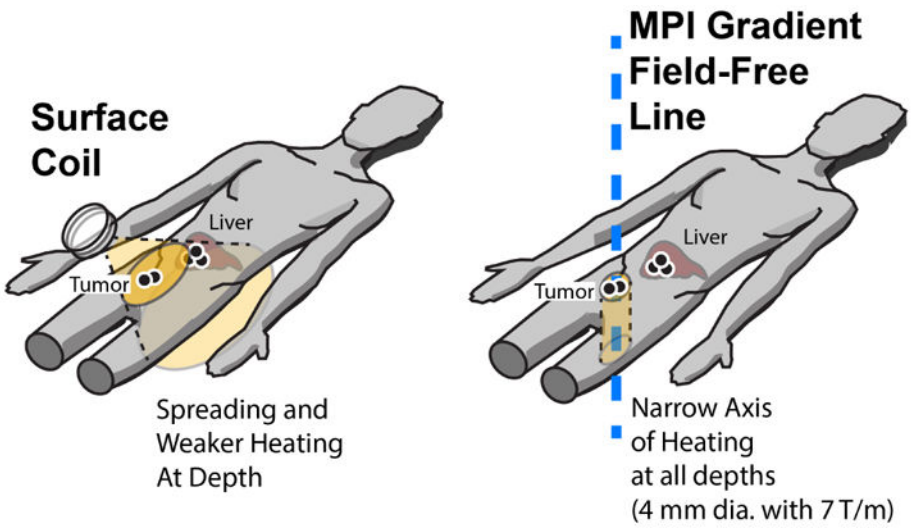

Figure 3.

Illustration of MPI-localized heating in the tumor while sparing the liver. This is compared to a surface coil method that can localize excitation near the body surface, but is unable to maintain narrow excitation deep within the body due to the field spreading and drop-off with distance. Furthermore, since $\lambda/2 \approx 50$ m for typical heating frequencies, the excitation field cannot be focused into a narrow spot. Collateral damage may done to healthy tissues with non-specific SPION accumulations i.e. clearance organs. In contrast, MPI gradients localizes heating by a completely different mechanism, which is to suppress nanoparticle rotation rather than shaping the excitation wave. Like MPI which can image at depth, heating is localized to the field-free-line (narrow axis) without spreading or attenuation with depth. With a 7 T/m gradient, localization to within a 4 mm diameter cylinder is expected.

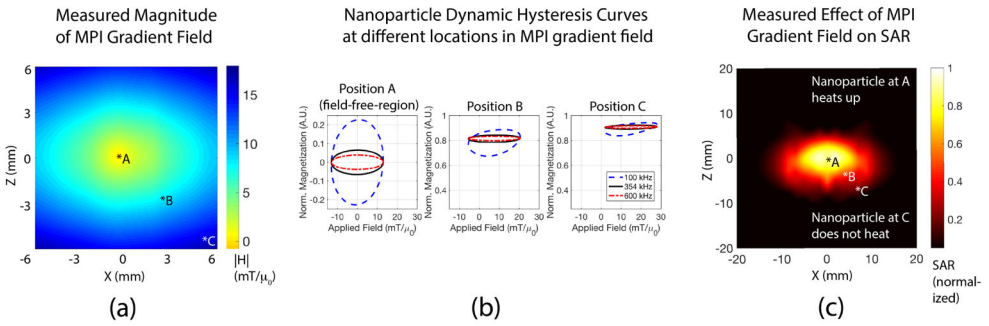

Figure 4.

Experimental results demonstrating the mechanism behind MPI gradient-based localization of heating.(a) Magnitude of the MPI gradient in the x-z plane (Lakeshore™Gaussmeter). The gradient field has zero magnetic field at the center and a high magnitude everywhere else. Due to the field-free-line geometry along the y-axis, each x-z slice along y has the same magnetic field profile. (b) SPION dynamic hysteresis loops was simulated at different positions in the gradient field. The hysteresis loops are most open at position A (|H| = 0) while the hysteresis loops are closed at other positions. Because heating depends on the area bounded by the hysteresis loop, the gradient field localizes heating to the field-free-line where |H| ≈ 0. Different drive frequencies have the same trend, showing that this localization method is flexible and works for a range of MPI drive fields. (c) Nanoparticles were put at different locations in the gradient field and heated with 354 kHz, 13 mT excitation. (see Methods: Heating Localization Characterization for details) The measured temperature rise and SAR (Neoptix™probes) is observed to be highest when the nanoparticle is located at position A (field-free-line), in line with simulations in (b). Heating was suppressed at other positions due to the large |H| away from the field-free-line. The 2.35 T/m gradient used here localizes heating to within a 7 mm radius region, but doubling the gradient to 7 T/m will improve localization to 2.3 mm radius.

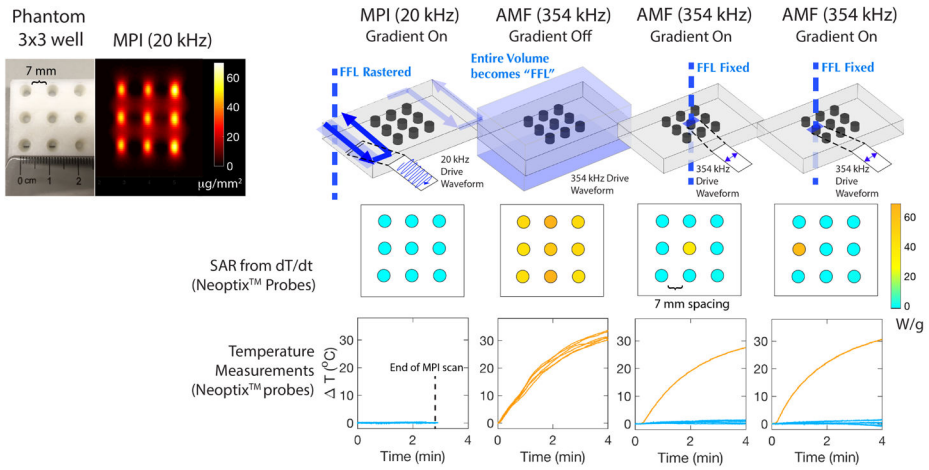

Figure 5.

In vitro experimental demonstration of localization of magnetic hyperthermia. A 3 × 3 grid phantom was used where each well was filled with 100 μl of 25 mg/ml SPIONs. The temperature of each well was measured by Neoptix™fiber optic temperature sensors under different imaging or heating conditions. During a standard MPI scan, no heating was observed due to the low frequency (20 kHz) and raster trajectory. During a high frequency (354 kHz) heating scan without MPI gradients, all the wells heat up. When the MPI gradients are used, the user is able to selectively heat up only the well where the field-free-line is located, with negligible heating in all neighboring wells. Because the wells are spaced 7 mm apart, we demonstrated that heating is localized to within 7 mm for a 2.35 T/m MPI gradient. Higher gradients at 7 T/m can improve this value to 2.35 mm.

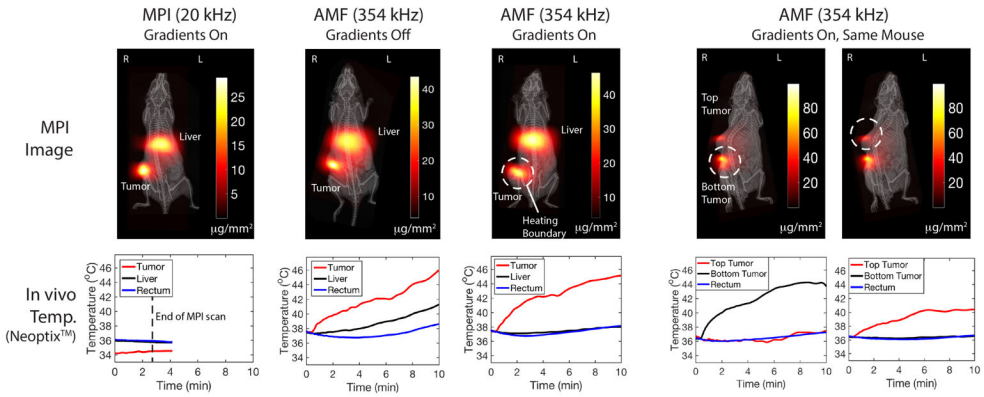

Figure 6.

In vivo experimental demonstration of localization of magnetic hyperthermia. The tumor was heated while sparing the liver. All *in vivo* local temperatures were measured by Neoptix™fiber optic temperature sensors. During a standard MPI scan, negligible heating was observed in the mouse to the low frequency (20 kHz) and raster trajectory. During a high frequency (354 kHz) heating scan without MPI gradients, all *in vivo* locations with nanoparticles heat up (thus damaging the healthy liver). When the MPI gradients are used, only the tumor is heated while the liver is spared. Lastly, we used a dual tumor mouse to demonstrate arbitrary user control of which tumor to heat. We first centered the field-free-line over the bottom tumor. Only the bottom tumor heated up while the top tumor was spared. Subsequently, without removing the mouse, we shifted the field-free-line over the top tumor. Only the top tumor heated up while the bottom tumor was spared, demonstrating arbitrary control of the site of heating just by shifting the MPI field-free-line.

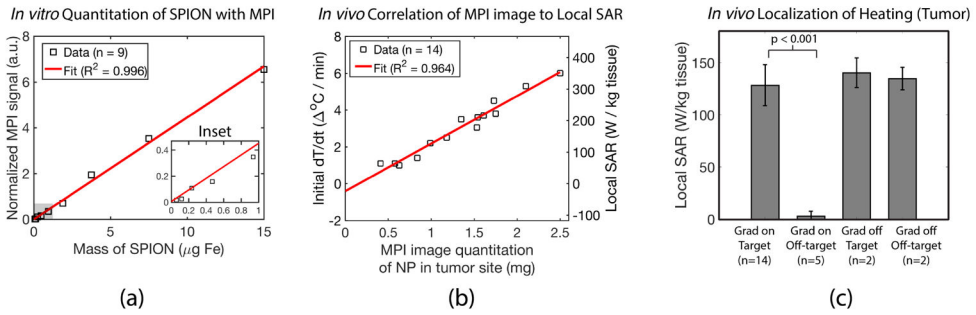

Figure 7.

Experimental demonstration of MPI's potential for dose planning, image guidance and actuation localization. See "Methods - MPI characterization" for set-up details. (a) *In vitro* data showing the MPI image is linearly quantitative (R^2 = 0.996) for the amount of SPION. (b) The *in vivo* MPI image intensity is well correlated (R^2 = 0.964) with the deposited SAR measured *in vivo*, enabling dose planning and image guidance. (c) Localization of the heating to the targeted location is demonstrated *in vivo* with p-value of < 0.001 (Welch's t-test, n = 14). Localization is clearly attributed to the MPI gradient, since there is no localization of heating when the gradients are off. This suggests that MPI gradients can reliably spare the liver while treating the tumor 1 – 2 cm away.

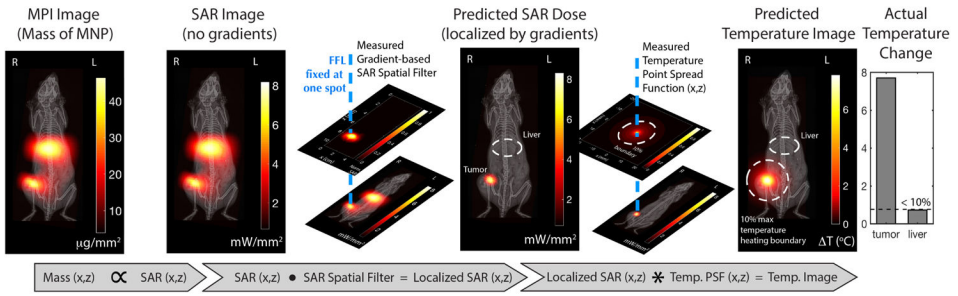

Figure 8.

Experimental demonstration that MPI can predict the spatial distribution of heating for image-guided, gradient-localized magnetic hyperthermia. Because MPI is quantitative for the mass of SPION, and since SAR is proportional to the SPION mass, we can obtain a SAR image from the MPI image (no gradients and localization yet). To predict the localization effect of the MPI gradients, we dot multiply the SAR image with suppression effect of the MPI gradient which is in essence a SAR spatial filter. We thus obtain a prediction of the SAR dose after gradient localization. Finally, to account for heat spreading through tissue from the SPION mass, we convolve the previous image with a temperature spatial point spread function (PSF). Our predicted spatial distribution of heating matches experimental data in that the liver was heated by less than $0.8°C$ as predicted by the calculated temperature map.

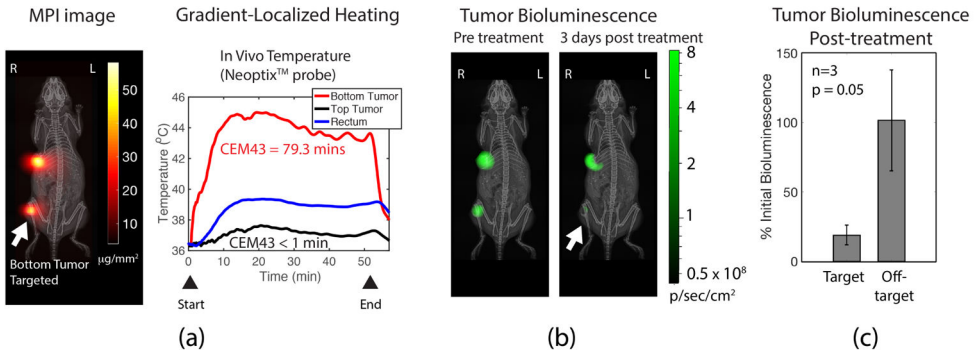

Figure 9.

Experimental assessment of localized heat therapy using a bioluminescence-competent MDA-MB-231-luc xenograft model. (a) MPI image of the dual tumor MDA-MB-231-luc xenograft mice. The bottom tumor is targeted during gradient-localized heating. *in vivo* temperature at both tumors and the rectum measured by NeoptixTM fiber optic temperature probes. The greatest heating occurred in the targeted bottom tumor, while the upper tumor received negligible heating. The total CEM43 achieved was 79.3 minutes in the targeted bottom tumor. The core body temperature, however, was slightly elevated and likely due to the homeostatic response distributing heat from the heated bottom tumor to the rest of the body. (b) Luciferase bioluminescence activity of the tumor was measured before and after treatment. The results show a greater than 6-fold decrease in activity for the treated bottom tumor, while the untreated tumor had almost no change in bioluminescence activity. Thus, this demonstrates the utility of MPI gradients in localizing tumor therapy. (c) Statistics (n = 3, p-value = 0.05 with Welch's t-test) show localization of therapy to the tumor while sparing off-target sites.

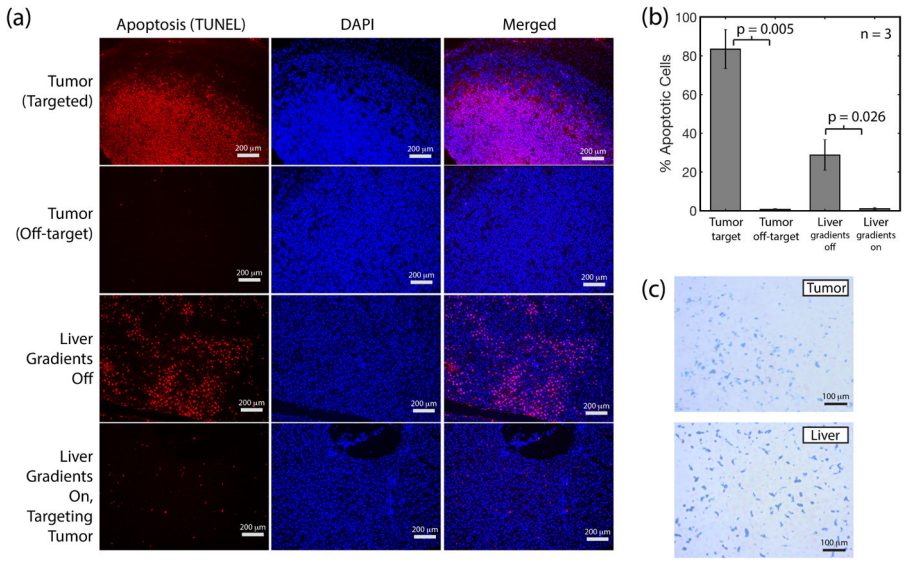

Figure 10.

Histological assessment of MPI localization of thermal damage. (a) Apoptosis assay (red) and DAPI stain (blue) shows apoptosis only occurs in the targeted tumor but not in the neighboring off-target tumor, verifying localization of heat damage by the MPI gradients. The liver is also damaged when MPI gradients are turned off and uniform heating of the tumor and all other locations occurs. In contrast, no damage is observed in the liver when the MPI gradient is turned on and targeted at the tumor. (b) Statistics (n = 3, p-value = 0.005 with Welch's t-test) show localization of thermal damage by MPI gradients. The liver sustains damage if MPI gradients are off due to collateral heating of the SPIONs cleared to the liver. In contrast, the liver is negligibly damaged if MPI gradients are on (p-value = 0.026). These results validate the ability of MPI gradients to localize thermal damage to the tumor while sparing the liver 1 – 2 cm away. (c) Prussian Blue stain confirms that SPIONs are successfully delivered to both the tumor and liver (clearance organ).

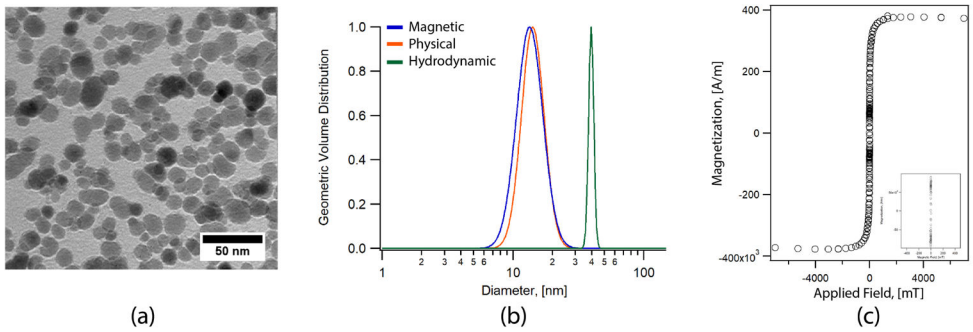

Figure 11.

Experimental characterization of the magnetic nanoparticles used in this study. The nanoparticles are PEG coated, single crystalline core, superparamagnetic iron oxide. (a) TEM of the nanoparticles. (b) Histogram of the core size distribution gives a nominal core size of 13 nm with effective magnetic core size of 11.7 nm. DLS analysis of the hydrodynamic diameter with number weighted distribution gives a value of ~ 40 nm. (c) Magnetization response of the SPIONs. Inset shows a zoom in of the region close to zero field.

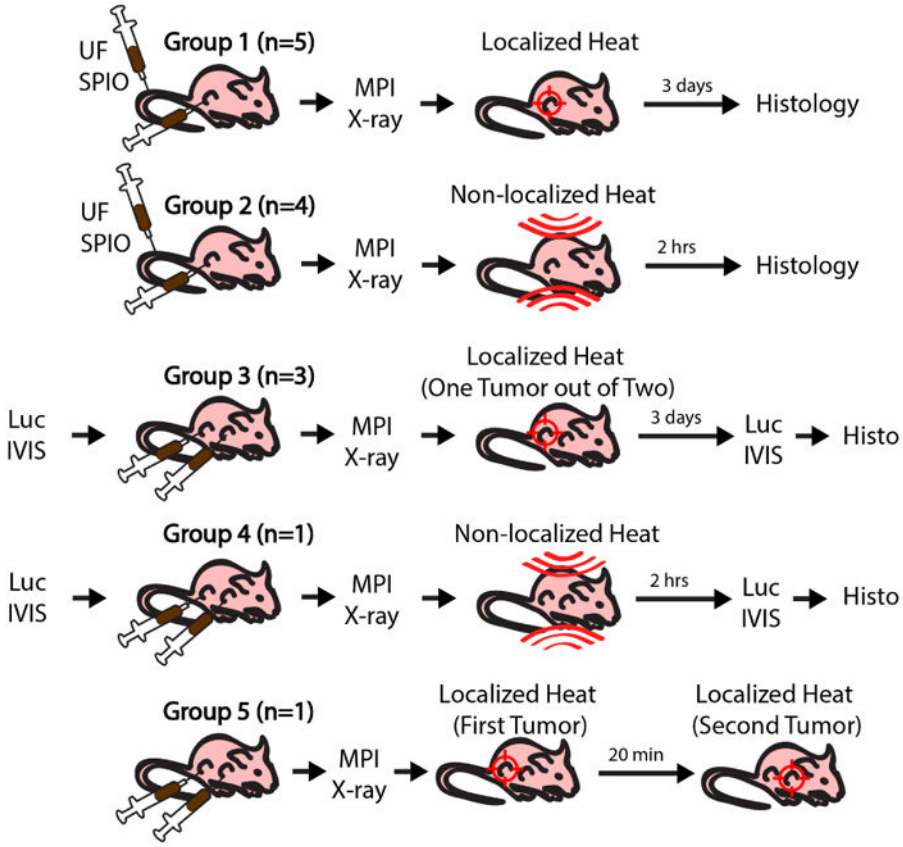

Figure 12.

This study used 5 groups of athymic nude mice. Groups 1 and 2 had a single U87MG xenograft and received tail vein injections and intratumoral injection of 1.25 mg Fe SPION each. Bioluminescence imaging was performed for groups 3 and 4 that had luciferin-competent dual MDA-MB-231-luc xenografts (each intratumorally injected with 1.25 mg Fe SPION). Group 5 had a double U87MG xenograft and received intratumoral injection of 1.25 mg Fe SPION in each tumor. MPI and projection X-ray was performed for all groups. Groups 1 & 3 had gradient-localized heating while Groups 2 & 4 had gradient-localization off during heating. Group 5 had gradient-localized heating that sequentially targeted one tumor then another. For all groups, post-euthanasia, the liver and tumor were excised for histology.